PHYSICAL REVIEW E **92**, 052714 (2015)

Totally asymmetric simple exclusion process simulations of molecular motor transport on random networks with asymmetric exit rates

D. V. Denisov, D. M. Miedema, B. Nienhuis, and P. Schall
Institute of Physics, University of Amsterdam, P.O. Box 94485, 1090 GL Amsterdam, The Netherlands

(Received 17 June 2015; revised manuscript received 27 August 2015; published 19 November 2015)

Using the totally asymmetric simple-exclusion-process and mean-field transport theory, we investigate the transport in closed random networks with simple crossing topology—two incoming, two outgoing segments, as a model for molecular motor motion along biopolymer networks. Inspired by *in vitro* observation of molecular motor motion, we model the motor behavior at the intersections by introducing different exit rates for the two outgoing segments. Our simulations of this simple network reveal surprisingly rich behavior of the transport current with respect to the global density and exit rate ratio. For asymmetric exit rates, we find a broad current plateau at intermediate motor densities resulting from the competition of two subnetwork populations. This current plateau leads to stabilization of transport properties within such networks.

DOI: 10.1103/PhysRevE.92.052714 PACS number(s): 87.16.−b, 05.60.Cd, 64.60.aq

I. INTRODUCTION

Transport of matter and energy is essential for maintaining complex structures. A constant driving can create and maintain the order in man-made structures as well as in living organisms. In fact, efficient transport is crucial for people living in modern societies: food, building components, energy, and people themselves are transported daily between rural and urban areas. Similarly, on the subcellular level, nutrition and molecular building blocks are transported from the periphery of the cell to its core [1–3]. Motor proteins move actively along the filament network, which also acts as cytoskeleton of the cell [4–8]. In both cases, maintaining a robust transport is crucial, in particular with respect to variations in density. In many transport systems, the transport is carried out by unidirectional movement of carriers (e.g., trucks, molecular motors, etc.), along networks consisting of linelike pathway segments and crossings. Such unidirectional particle motion has been modeled by the well-known totally asymmetric simple exclusion process (TASEP) [9–11], which has recently been applied to transport along cytoskeleton assemblies [12,13]. Originally formulated for one-dimensional systems [14], TASEP was extended to networks by defining the dynamics at crossings. These previous works discuss in detail the role of network structure in the modeling of complex traffic problems [12,13].

Yet, recent experimental observation of molecular motor motion highlights the nontrivial dynamics of molecular motors at crossings: specific types of motors were found to switch between segments with specific probabilities [15–19]. This preference at crossings might crucially determine the transport properties of the network. Earlier TASEP simulations of large networks [12,13] used symmetric exit rates, and only recent simulations of a *single* crossing show the heterogenous motor density that can arise from a preference in outflow directions among the crossing filaments [20,21].

Here, we study the role of asymmetric exit rates on the transport behavior of large networks using the TASEP model. Inspired by *in vitro* experiments, in which typically arrays of cytoskeleton filaments are created by attachment to a surface, we focus on a network topology of intersecting lines in a two-dimensional plane: in this topology intersections consist of a single crossing of two filaments. We show that interesting heterogeneous network densities and network transport arises from the local asymmetric exit rates. These exit rates, together with the global motor density crucially determine the transport capacity of the network. We identify four regimes of current-density behavior: A low-density regime controlled by the relative exit probabilities and network topology, a jamming regime with heterogeneous density and resulting complex interplay of subnetwork currents, a saturation regime, and a high-density regime with local dynamics and homogenous density. The extent of each regime and the actual value of the current is found to strongly depend on the relative exit rates at crossings.

II. MODEL DESCRIPTION

We model cytoskeleton assemblies with a two-dimensional network of intersecting segments. Inspired by *in vitro* experiments, where the cytoskeleton is typically grown by sedimenting filaments on a glass plate [Fig. 1(a)], we create a network topology by projecting lines with random positions and directions on a square [Fig. 1(b)]. The part of a line (filament) between two crossings is defined as a segment. Every segment has 1D structure consisting of L lattice sites. Each site can accommodate maximally one motor. The motors can move from site to site along one direction only, which is defined randomly, and once defined, is fixed during the entire simulation run. For simplicity we define a uniform length L for all segments; we found that this produces more robust results while not affecting the general transport behavior through the network [22]. We introduce periodic boundary conditions by connecting the beginning and end of every line at the boundaries of the square, thus creating a closed network. The resulting network is characterized by the number of crossings N_v, the number of segments $N_s = 2N_v$, and the total number of sites $M_s = (2L - 1)N_v$. The network is subsequently populated with motors at a density ρ, defined as the ratio of the total number of motors and the total number of sites M_s.

Molecular motor motion is modeled with the TASEP, in which particles perform unidirectional random sequential hops constrained by the fact that they may not overlap with

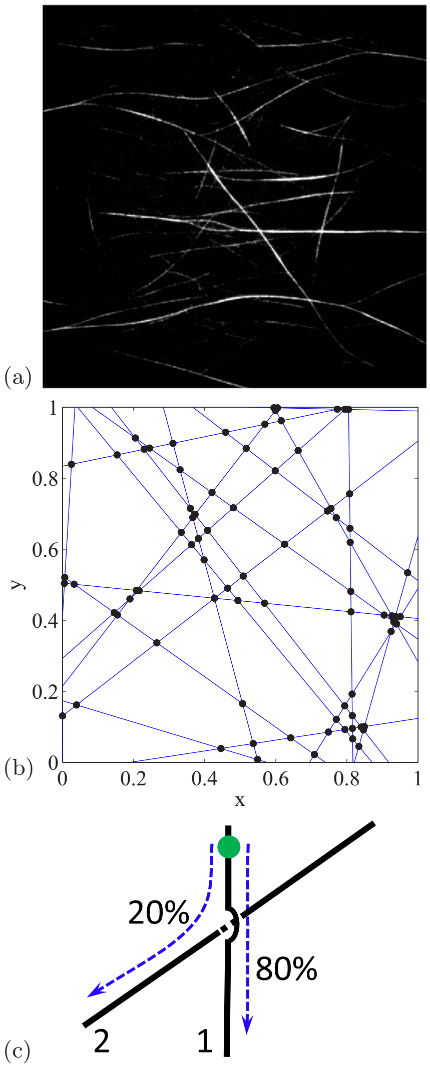

FIG. 1. (Color online) (a) Experimentally obtained microtubule network. (b) Simulated network. (c) Sketch of crossing with probable particle paths corresponding to $\gamma = 0.8$.

each other. During a single update, a motor advances one site forward if the target site is unoccupied; otherwise, no progression occurs. Network sites are updated in random sequential order and one update cycle corresponds to M_s single-site updates.

When a motor arrives at the crossing, it continues with probability γ along one outgoing segment and with probability $1 - \gamma$ along the other, *independently* of the incoming segment. As shown in Fig. 1(c), this can account for the local topology of *in vitro* biopolymer networks, where the preferred filament (overpass filament 1) is lying "on top" of the other filament (underpass filament 2). The probability γ thus defined for every crossing is kept constant during the simulation, and is hence a fixed property of the network. Our approach is based on the experimental observation [15] that motors with cargo bead attached are more likely to stay on the overpass filament and change direction when traveling on the underpass filament, making the overpass filament always preferable [23]. For simplicity, we define equal γ for all crossings independent of the history of motor motion. For completeness, consequences of history-dependant motor motion are discussed in Appendix C.

Finally, we neglect the possible unbinding of motors, which is observed in Refs. [15,24], and studied in simulations by Neri *et al.* [13]. Such unbinding weakens the correlations in the traffic flow of the motors. However, it was shown that for motors with attached cargo bead [15] the unbinding probability at the crossings is small or negligible. Neglecting unbinding allows us to focus on the physical effects of jamming and flow [25] and obtain a simple physical picture in terms of γ. The control parameters of our simulations are thus the exit probability γ, which due to the symmetry we choose as $0.5 \leqslant \gamma \leqslant 1$, and the global motor density $0 < \rho < 1$. We consider relatively large networks with $N_s \sim 500$ and uniform segment length $L = 500$. All data have been averaged over 10 000 cycles in steady state, after discarding the transient (initial ~3000 cycles).

III. RESULTS

The effect of exit probability γ on the network current is shown in Fig. 2, where we plot the total current versus density ρ for various values of γ (blue solid curves). For comparison, we also show the mean-field current through a single segment $J_s = \rho(1 - \rho)$ (black dashed line) [26] that exhibits a maximum at $\rho = 0.5$ due to competition of growing density increasing the current and density-induced jamming reducing it. The network current behaves similar to that of a single segment for symmetric exit rates ($\gamma = 0.5$, upper blue solid curve in Fig. 2): it is symmetric around $\rho \sim 0.5$ and deviates from that of the single segment only at densities around 0.5. The situation changes for asymmetric exit probability ($\gamma \neq 0.5$), where the network current becomes asymmetric and progressively reduces and flattens with increasing γ, until at $\gamma \sim 0.9$ when it becomes largely independent of density. Thus, the asymmetric exit probability reduces the network current and stabilizes it at the same time.

How does this emerging current plateau arise from the interplay of currents in the network? To answer this question

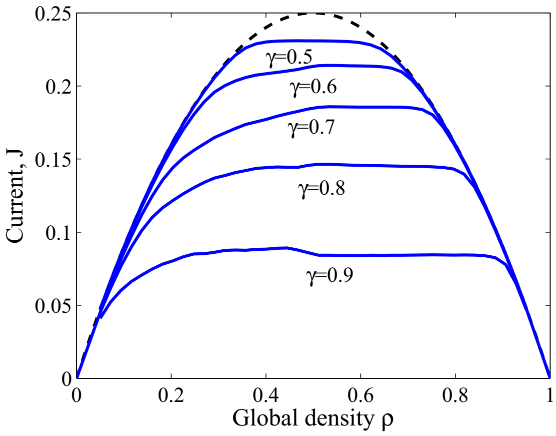

FIG. 2. (Color online) Transport current J dependence on global density ρ for different exit probabilities γ obtained from the TASEP simulations. Dashed black curve is shown for comparison with the current through single segment. Data is averaged over 10 000 cycles after waiting for 3000 cycles to reach steady state.

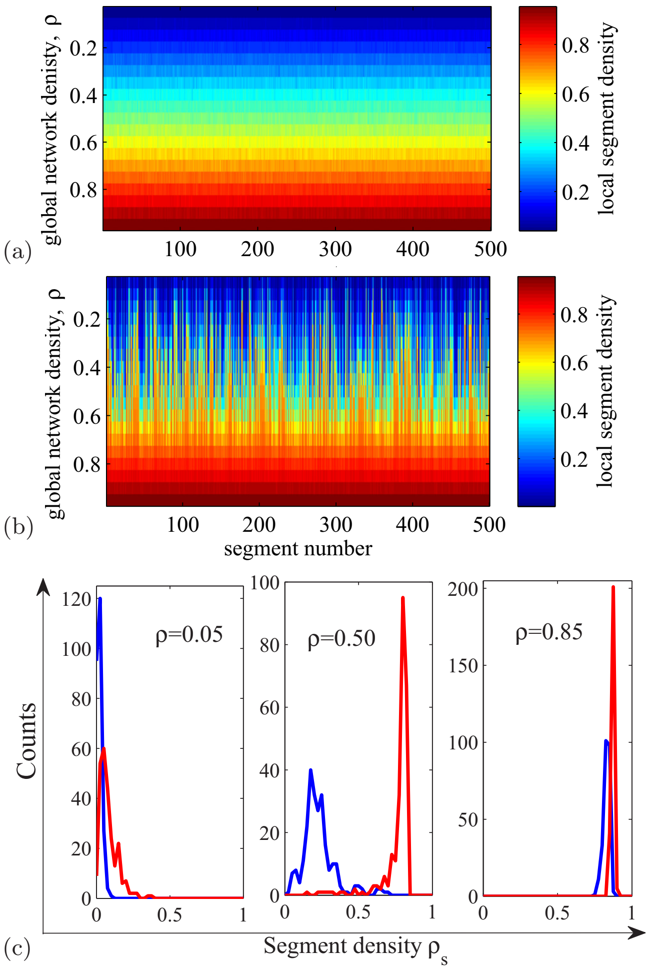

FIG. 3. (Color online) Local density distribution (shown by color) in segments (horizontal axis), depending on average global density ρ (vertical axis). (a) $\gamma = 0.5$, homogenous distribution. (b) $\gamma = 0.8$, heterogenous distribution. (c) Histograms of density distributions for $\gamma = 0.8$ for high-preferability segments are shown by the red (light gray) curve, and for low-preferability segments are shown by the blue (dark gray) curve. The three panels show different global densities ρ. Large difference in the distribution occurs for the intermediate density.

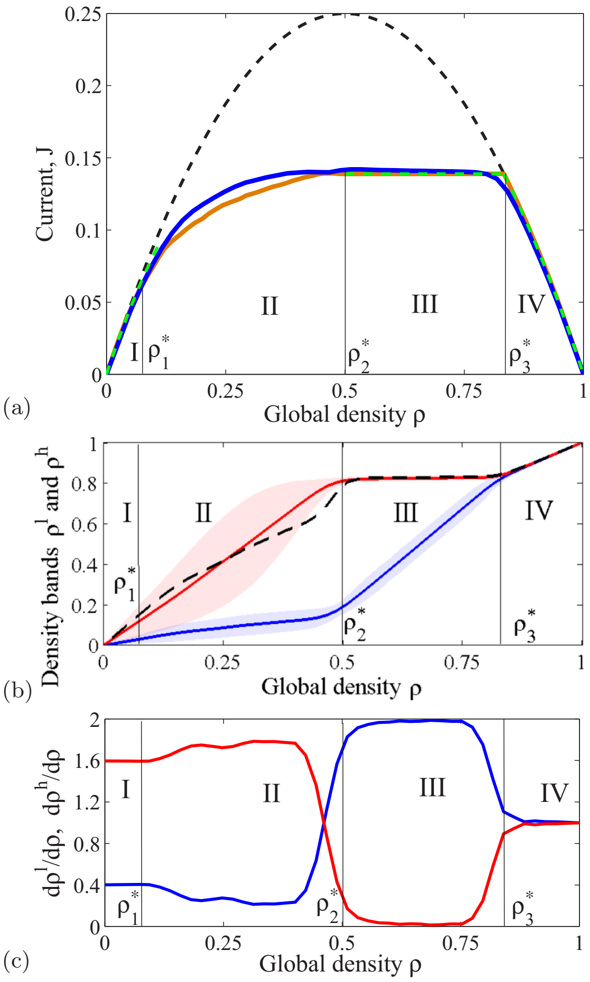

FIG. 4. (Color online) (a) Transport current J for $\gamma = 0.8$ calculated using TASEP model is shown by the blue (dark gray) curve and calculated using iteration method is shown by the brown (light gray) curve. Homogeneses current distrusting $J_s = \rho_s(1 - \rho_s)$ through a single segment is shown by dashed black curve. Dashed green (light gray) lines show approximate solution obtained using two subnetwork approach. (b) Dependence of mean densities in low- $\langle \rho^l \rangle$ and high-preferability $\langle \rho^h \rangle$ bands on the global density ρ is shown by the blue (dark gray) and red (light gray) color, respectively. Shaded blue and red areas show the density distribution within the bands. Dashed black curve shows the mean density of crossings $\langle \rho_v \rangle$. (c) Derivatives $\partial \langle \rho^h \rangle / \partial \rho$ and $\partial \langle \rho^l \rangle / \partial \rho$ corresponding to mean growth rates in high- and low-preferability subnetworks are shown by the red (light gray) and blue (dark gray) color, respectively. In all figures ρ_1^*, ρ_2^*, and ρ_3^* show transitions between different regimes.

we investigate the distribution of individual segment densities ρ_s. We compare density distributions for symmetric and asymmetric exit probability in Fig. 3. For $\gamma = 0.5$, the density is homogeneous across the entire network: local and global densities largely coincide with only minor variation across segments [Fig. 3(a)]. For $\gamma = 0.8$, in contrast, we find strong inhomogeneity at intermediate global density [Fig. 3(b)]: the asymmetric exit probability leads to redistribution of paths and resulting redistribution of segment densities. Indeed, the asymmetric exit probability redistributes the motors into two subsystems: associated with the vertex exit probabilities, the network can be considered as consisting of two interconnected subnetworks, one consisting of segments with entry probability γ and the other consisting of segments with probability $1 - \gamma$. The subnetwork with higher entry probability should populate faster, leading to the heterogeneous distribution of densities shown in Fig. 3(b). This is indeed confirmed in the subnetwork density distributions as shown in Fig. 3(c): at intermediate ρ, the density of the high-preferability subnetwork has grown much more, as reflected in the shift of the distribution to higher density. Due to interplay of the individual segments, the density within each subnetwork is heterogeneously distributed.

To link this density evolution to the total current, we plot average densities of the two subnetworks together with the total current in Figs. 4(a) and 4(b). Clearly, the high-preferability subnetwork takes up particles at a faster rate as shown in Fig. 4(b); this is a direct result of the higher entry probability.

The initial slopes of the growing densities in high- and low-preferability subnetworks are 2γ and $2(1-\gamma)$, respectively, reflecting the two entry probabilities. When roughly half of the network sites are occupied ($\rho \sim 0.5$), high-preferability segments become saturated, and particles are increasingly taken up by the low-preferability segments. This interplay of the two subnetworks leads to stabilization of the total network current: as we will see below, jamming effects in the high-preferability subnetwork lead to an emerging state in the low-preferability subnetwork with rapidly changing density but constant current, which ultimately leads to the current plateau as demonstrated in Fig. 4(a). This change of contributions is most clearly reflected in the derivatives of the densities as shown in Fig. 4(c); it qualitatively explains the stabilization of current in the network. While the current is reduced, it becomes largely independent of density. At even higher density, the network becomes homogeneous and the difference between subnetworks vanishes; see Fig. 4(b). Hence, our approach to reduce the network into two interfering subnetworks allows us to understand the network behavior qualitatively.

Using basic relations for single segments, we can also model the network transport properties quantitatively. The mean current is given by $J = \frac{1}{N_s}\sum J_s$, where the single-segment current $J_s = \rho_s(1-\rho_s)$. Provided segments are sufficiently long ($L >> 1$) to neglect boundary effects, the segment density ρ_s is determined solely by the incoming rate, $0 \geqslant \alpha \geqslant 1$, and outflow rate, $0 \geqslant \beta \geqslant 1$ [26], which are themselves determined by the densities at the vertices ρ_v. For the inflow rate, $\alpha = \rho_v\gamma$ or $\alpha = \rho_v(1-\gamma)$, while the outflow rate $\beta = 1-\rho_v$, controlled solely by the availability of an empty exit vertex.

For single segments, it is known that if particles come in at a lower rate than they leave the segment ($\alpha < \beta$), then $\rho_s = \alpha < 0.5$. If particles flow out at a lower rate than they come in ($\beta < \alpha$), then the segment is jammed, and $\rho_s = 1-\beta > 0.5$. The resulting currents are then $J_s = \alpha(1-\alpha)$ and $J_s = \beta(1-\beta)$, respectively. If $\alpha = \beta < 0.5$, then two regimes (free flowing and jammed) coexist in one segment, separated by a moving domain wall: in the beginning, the segment will be inflow controlled with density $\rho_s = \alpha$, and in the end it will be outflow controlled with $\rho_s = 1-\alpha$ [26]. Since $\alpha = \beta$, the current is constant during this density increase, being $J_s = \alpha(1-\alpha)$. In the rare case of $\alpha > 0.5$ and $\beta > 0.5$, the current goes to its maximum $J = 0.25$.

Using these local relations for segment currents, we can now compute the average steady-state current of the network. We do this by using an iterative method to converge density and current; see Appendix A. The resulting steady-state current shown by the brown (light gray) solid line in Fig. 4(a) reproduces all features of the TASEP simulations. This close correspondence lends credence to the model. We will show in the following that a further simplification to average subnetwork densities allows for a surprisingly good description of the network behavior. We represent the two subnetworks by their average density $\langle\rho^h\rangle$ and $\langle\rho^l\rangle$ and the corresponding subnetwork currents by J^h and J^l. This allows physical insight into the transport behavior of the network and its dependence on γ. We distinguish four regimes as a function of increasing density as discussed below.

1. Linear regime

At low density, currents in the two subnetworks are determined solely by the entry rates γ and $1-\gamma$. The average subnetwork densities grow as $\langle\rho^h\rangle = 2\gamma\rho$ and $\langle\rho^l\rangle = 2(1-\gamma)\rho$, from which we can directly compute the subnetwork currents J^h and J^l using $J_s = \rho_s(1-\rho_s)$. The resulting total current is $J = 1/2(J^h + J^l) = \rho(1-\rho) - \rho^2(1-2\gamma)^2$ [dashed green line in Fig. 4(a)], where the first term indicates the current for homogeneous density distribution, and the second term reflects the current reduction due to density redistribution between the two subnetworks. This term vanishes for $\gamma = 0.5$, for which the density distribution becomes homogeneous. Note that the real reduction is slightly lower than given by the term $\rho^2(1-2\gamma)^2$ due to the distribution of subnetwork densities around the mean.

This low-density linear regime holds up to some critical density ρ_1^*, at which the most populated high-preferability segment becomes jammed ($\alpha \geqslant \beta$) and the density $\langle\rho^h\rangle$ grows faster than linear as shown by the derivatives in Fig. 4(c). We can explicitly calculate ρ_1^* from the structure of the network with the help of the transition matrix ϵ_{ij}, which describes transition rates between vertices i and j. Since for $\rho < \rho_1^*$ all segments are inflow controlled, transitions between two neighboring vertices will occur with rate either γ or $1-\gamma$, allowing us to linearize ϵ_{ij} and find exact values of ρ_v for every vertex, which are linearly proportional to ρ (see Appendix B). Knowing ρ_v we can compute all ρ_s and consequently the exact value of current through the whole network. Moreover, for every particular network we can explicitly solve the condition $\alpha \geqslant \beta$ ($\gamma\rho_v' \geqslant 1-\rho_v''$) for every segment to find the exact $\rho = \rho_1^*$ when the first segment becomes jammed. Averaging over many random networks, we find $\rho_1^* \approx \frac{\rho_1^0}{(N_s/2)^{|\gamma-0.5|}}$ (with $\rho_1^0(\gamma) \sim 1/3$, see Appendix B); using $N_s = 500$ and $\gamma = 0.8$, we obtain $\rho_1^* \approx 0.07$, which locates the transition well, as shown in Fig. 4(c). It is interesting to note that for sufficiently large networks ($N_s \to \infty$) and high anisotropy ($\gamma \neq 0.5$) this transition density $\rho_1^* \to 0$, indicating that jamming effects start to occur already at infinitely small densities.

2. Jamming regime

Above ρ_1^*, jamming will spread to neighboring high-preferability segments in the direction *opposite* to the local currents, similar to jam propagation opposite to vehicle motion in traffic [27,28]. Since for the single segment, the transition from the unjammed ($\rho_s = \alpha$) to the jammed state ($\rho_s = 1-\beta$) is quite abrupt for $\alpha \approx \beta < 0.5$, the jam propagation is accompanied by a nonlinear growth of $\langle\rho^h\rangle$, which is compensated by a slightly stagnating growth in the low-preferability subnetwork $\langle\rho^l\rangle$, as shown by the derivatives in Fig. 4(c).

With the gradual propagation of jams, the density in the high-preferability subnetwork becomes increasingly heterogeneous as demonstrated by the red shaded area in Fig. 4(b). This heterogeneity reaches a maximum in the middle of the jamming regime and diminishes again as large fractions of high-preferability segments become jammed and as a result their densities equalize. Eventually, at the end of the jamming regime defined by $\rho = \rho_2^*$ all high-preferability segments become saturated, and their density does not grow any further [see Figs. 4(b) and 4(c)].

Toward the end of the jamming regime ($\rho = \rho_2^*$) all high-preferability segments and connected vertices are saturated with equal particle density, $\rho_s^h = \rho_v = 1 - \beta$. At the same time, the low preferability segments are still unjammed. Hence, at ρ_2^*, the density difference between the two subnetworks is maximal.

3. Saturation regime

Above ρ_2^*, the density in the high-preferability subnetwork no longer increases, and further increase of ρ takes place in the low-preferability subnetwork, where consequently jams start to form. Since high- and low-preferability segments are connected by the same vertices, vertices with saturated uniform density ρ_v control the inflow [$\alpha = \rho_v(1-\gamma)$] and outflow ($\beta = 1 - \rho_v$) of low-preferability segments. The only regime where the segment density ρ_s^l can rapidly change while inflow and outflow rates remain constant is during the shock phase [26], when jammed and free flow coexist within one segment and $\alpha = \beta$. Using this equality for the low-preferability segments, we obtain $\rho_v = 1/(2-\gamma)$. This allows us to calculate the saturating current of high-preferability segments: using $J^h = \beta(1-\beta)$ with $\beta = 1 - \rho_v$, we obtain $J^h = (1-\gamma)/(2-\gamma)^2$. Since in the low-preferability segments, jam and free flow coexist, $\langle \rho^l \rangle$ changes from $\alpha = (1-\gamma)/(2-\gamma)$ to $1 - \beta = 1/(2-\gamma)$ with increasing ρ, corresponding to 1/6 and 5/6 for $\gamma = 0.8$, again in agreement with the simulations. During this rapid density change, the low-preferability subnetwork current remains constant $J^l = \beta(1-\beta)$. The resulting total current is thus $J = 1/2(J^h + J^l) = (1-\gamma)/(2-\gamma)^2$ [dashed green line in Fig. 4(a)], independent of ρ, manifesting the current plateau.

Indeed, the TASEP simulations show plateau-like behavior with current values only slightly higher than the value $(1-\gamma)/(2-\gamma)^2$ [for $\gamma = 0.8$ in Fig. 4(a) the TASEP simulations plateau value is $\sim$0.141 while $(1-\gamma)/(2-\gamma)^2 = 0.139$]. Again, this small discrepancy results from the spread in densities within the subnetworks opposed to the fixed average densities $\langle \rho^l \rangle$ and $\langle \rho^h \rangle$ assumed here.

The transition density ρ_2^* at the start of the saturation regime can be estimated from the requirement that for $\rho \geqslant \rho_2^*$, all high-preferability segments are jammed; i.e., $\langle \rho^h \rangle = 1 - \beta = \rho_v = 1/(2-\gamma)$. At the same point all low-preferability segments are still unjammed, $\langle \rho^l \rangle = \alpha = (1-\gamma)\rho_v = (1-\gamma)/(2-\gamma)$; this leads to the mean density $\rho_2^* = (\langle \rho_s^l \rangle + \langle \rho_s^h \rangle)/2 = 0.5$, which is independent of γ.

By the end of the saturation regime at $\rho = \rho_3^*$, $\langle \rho^l \rangle$ has increased due to the jamming until $\langle \rho^l \rangle = \langle \rho^h \rangle = 1/(2-\gamma)$ and the density is homogenous throughout the whole network. This immediately gives the upper density of the saturation regime: $\rho_3^* = 1/(2-\gamma)$.

Interestingly, $\langle \rho^l \rangle$ remains much more homogeneous while rapidly increasing than $\langle \rho^h \rangle$ in the jamming regime [see blue and red shades in Fig. 4(b)]. This difference is a direct result of the vertex densities controlling the segment densities [see black curve in Fig. 4(b)]. During the jamming regime the crossing densities ρ_v evolve rapidly, while in saturation regime the crossing densities are saturated and fixed at $\rho_v = 1/(2-\gamma)$, thus creating density heterogeneities within segments rather than between them.

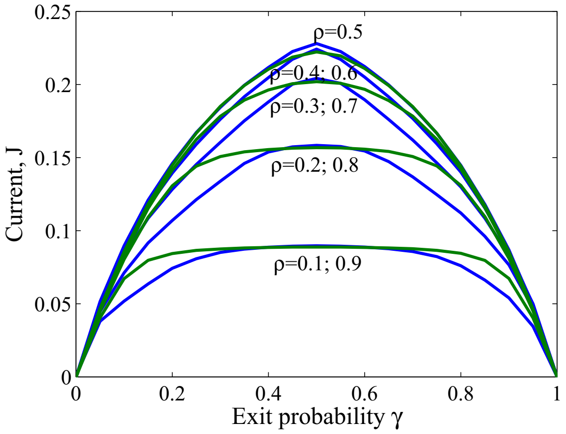

FIG. 5. (Color online) Transport current J dependence on exit probability γ for different densities ρ obtained from the TASEP simulations. Data is averaged over 10 000 cycles after waiting for 3000 cycles to reach steady state. Blue (dark gray) curves correspond to $\rho \leqslant 0.5$, green (light gray) ones to $\rho > 0.5$.

4. High-density regime

For $\rho > \rho_3^*$ the density in both high- and low-preferability segments is given by the outflow rate ($\beta = 1 - \rho_v$) and becomes independent of the exit probability γ. As a result, all segments behave identically $\rho_s^h = \rho_s^l = \rho_v = \rho$, as shown by the perfect overlap and the linear increase with slope 1 of the red (light gray) and blue (dark gray) curves in Fig. 4(b). The current is then simply $J = \rho(1-\rho)$, fitting perfectly with both TASEP simulation and iteration method [see dashed green line in Fig. 4(a)].

We finally show the explicit dependence of the current on exit probability γ in Fig. 5. Interestingly, a similar plateau behavior is observed as for the density dependence, indicating that the current is stabilized also with respect to γ: green (light gray) curves for $\rho > 0.5$ evidence the emergence of a plateau in J with increasing ρ. This plateau corresponds to the high-density regime; hence, its extension can be derived from ρ_3^*, and we obtain $1/\rho - 1 \leqslant \gamma \leqslant 2 - 1/\rho$. At low densities, on the other hand ($\rho < 0.5$), a somewhat narrower plateau emerges with decreasing ρ and becomes established for $\rho < 0.1$. This rather low density corresponds to the linear regime, i.e., for $\rho < \rho_1^*$. In this case, we can estimate the plateau value from $J = \rho(1-\rho) - \rho^2(1-2\gamma)^2$ by neglecting the second term for $\gamma \sim 0.5$. We thus obtain the plateau value $J = \rho(1-\rho)$, which appears in a narrow range of γ close to 0.5; see blue (dark gray) curve for $\rho = 0.1$ in Fig. 5.

IV. SUMMARY

Using TASEP simulations and mean-field theory on complex networks, we have studied the transport properties of large networks with asymmetric exit rates. We find that the transport current depends strongly on the relative exit probabilities and the global density that together determine the transport properties and density distribution of the network. Asymmetric exit rates lead to strong decrease of the transport current, but at the same time to emergence of a current plateau that stabilizes the current: this plateau makes the current largely independent of variations in particle density. Similar current stabilization is observed with respect to variations in exit probabilities when the density ρ is rather low or high.

The main mechanism underlying this complex network behavior is the splitting of the network into two subnetworks according to the exit probabilities γ and $1-\gamma$. This splitting into two subnetworks, together with the (random) topology of the network sets the complex transport pathways, which, at intermediate densities, lead to heterogeneous crowding of the network. The resulting four transport regimes—linear, jamming, saturation, and high-density—are characterized by the relative densities of the two subnetworks and the density distribution within each subnetwork. Former is determined by γ, latter by the network topology.

The topology and asymmetric exit probabilities used here mimic that of typical *in vitro* experiments in which molecular motors walking along biopolymer networks exhibit specific preference to proceed along a certain segment at filament crossings. Our work hence provides insight into how local motor dynamics affect the collective transport properties of a biopolymer network. However, important additional effects arise from the unbinding of real motors that is experimentally observed. Such detachment of motors can weaken the correlations and jamming effects that we observe in the simulations.

The work presented here complements simulations of network transport based on random bidirectional [29] and guided motion between nodes [30,31] that are more suitable for internet traffic and urban transport description. In these studies it was shown that jamming can occur at relatively low densities. In the current work, we have shown that the unidirectional exclusion process together with asymmetric exit rates leads to complex jammed states with heterogeneous steady-state densities and currents that can nevertheless be understood based on the simple interplay of two subnetworks. Due to the generality of the exclusion process in modeling transport and arrest phenomena, our results may provide generic insights into traffic jams and transport capacities of highway networks, biological networks, and other systems with similar unidirectional topology.

ACKNOWLEDGMENTS

The authors thank S. Roth for her support in the experiments and E. Peterman for useful discussions. This work was done as part of the Complexity Program of NWO (The Nederlandse Organisatie voor Wetenschappelijk Onderzoek).

APPENDIX A: ITERATIVE SOLUTION OF MEAN-FIELD MODEL

Here we provide an iterative solution of the mean-field model, which—as we will show below—reproduces the network behavior quantitatively and shows excellent agreement with the TASEP simulations. This iterative method computes steady-state segment currents from the density at the vertices.

For each segment, the inflow rate α is proportional to the density ρ_v of the entry crossing and the exit probability, i.e., $\alpha = \rho_v\gamma$ or $\alpha = \rho_v(1-\gamma)$ [26]. On the other hand, the outflow rate β is controlled solely by the availability of an unoccupied exit vertex, so that $\beta = 1-\rho_v$ independent of γ. The change of density of each vertex is given by particle influx due to the two incoming segments and outflow due to the two outgoing segments, similar to Ref. [12]

$$\frac{\partial\rho_v}{\partial t} = \sum_{v'} J_s(\alpha_{v'},\beta_v) + \sum_{v''} J_s(\alpha_v,\beta_{v''}), \tag{A1}$$

where v' sums over the two incoming segments and v'' over the two outgoing segments. Here, the segment current is $J_s = \alpha(1-\alpha)$ for $\alpha < \beta$ and $J_s = \beta(1-\beta)$ for $\beta < \alpha$. Since α and β are themselves related to the vertex density as described above, any change of vertex density will in turn influence the segment currents, which again change the crossing densities. We hence use an iterative method to find steady-state currents and vertex densities. By expressing $\rho_v(t+1) = \rho_v(t) + \partial\rho_v(t)/\partial t$, we can find steady-state configurations, for which $\partial\rho_v(t)/\partial t = 0$ for all vertices (t here is quantized time steps).

The resulting steady-state network current depicted by the brown (light gray) line in Fig. 4(a) reproduces all features of the total current: the initial linear and nonlinear increase, saturation, and the final decrease due to complete jamming of the network. The remaining slight difference between the TASEP simulations and the iterative solution is associated with the approximation $J_s = \rho_s(1-\rho_s)$, which is strictly true only for infinite segment lengths.

APPENDIX B: LINEAR REGIME LIMIT

In this section we compute the transition density $\rho = \rho_1^*$ that bounds the linear regime. The linear regime ends when the density of each subnetwork is no longer linearly proportional to the global density. To pinpoint ρ_1^*, we determine the transition matrix ϵ, whose elements ϵ_{ij} denote the transition probabilities from vertex i to j. We define element $\epsilon_{ij} = 0$ when vertex j is not connected directly to vertex i through one segment, $\epsilon_{ij} = \gamma$ when j is connected to i through a high-preferability segment, and $\epsilon_{ij} = 1-\gamma$ when j is connected to i through a low-preferability segment. This matrix specifies the transitions between vertices, giving the probability a particle continues from one vertex to the next; the eigenvector corresponding to eigenvalue 1 of matrix ϵ holds the relative distribution of densities ρ_v among vertices in steady state. Knowing the densities of all vertices we can calculate the densities of every segment ρ_s through incoming rate $\alpha = \gamma\rho_v'$ or $\alpha = (1-\gamma)\rho_v'$ and outgoing rate $\beta = 1-\rho_v''$. Actually, while using the transition matrix ϵ we have assumed that all segments are inflow controlled ($\alpha < \beta$) and not jammed, only then the transition rates between vertices will depend on γ only. Indeed at low global density $\rho \leqslant \rho_1^*$, the computed values of ρ_s are in excellent agreement with the TASEP simulation results, since the transition matrix gives an exact solution of the density distribution among segments as shown in Fig. 6(a). As the first segment becomes jammed, $\alpha > \beta$, the linear-regime ends and the density distribution is no longer given by the transition matrix; see Figs. 6(b) and 6(c).

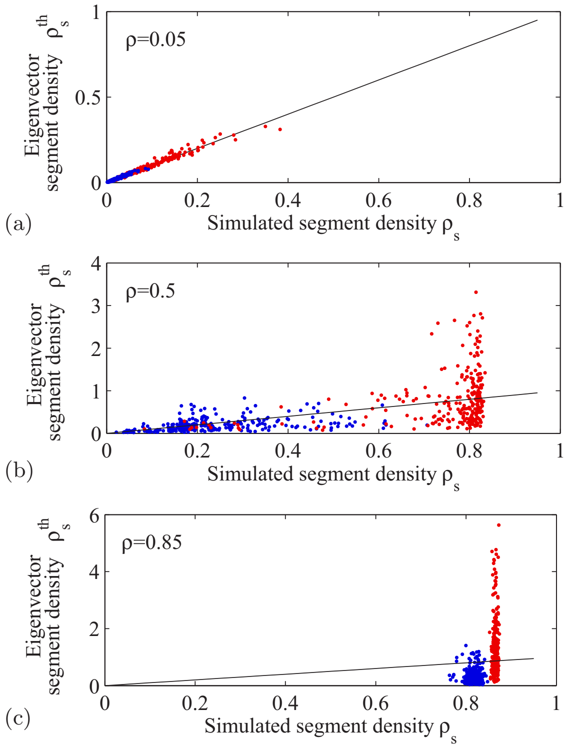

FIG. 6. (Color online) Comparison of segment densities obtained by TASEP simulations (horizontal axis) and transition matrix ϵ solution (vertical axis) for $\gamma = 0.8$. Every point represents the local segment density. Points lying along the black identity line "$y = x$" signify that both solutions are in agreement. Blue (dark gray) dots correspond to the low-preferability segments, red (light gray) ones to the high-preferability. (a) $\rho = 0.05$, excellent agreement between TASEP and ϵ solution. (b) $\rho = 0.5$, clear splitting between high- and low-preferability bands, only low-preferability segments are somewhat close to ϵ solution. (c) $\rho = 0.85$, low- and high-preferability segments are in jammed state, very close to each other.

The task to find the end of the linear regime is to find the lowest global density $\rho = \rho_1^*$ where $\alpha > \beta$ for one of the segments. For $\gamma = 0.5$ we can find a simple analytical solution, since in this isotropic case all segments and vertices are identical. By solving $\alpha > \beta \Leftrightarrow \gamma\rho_v > 1 - \rho_v$ we get $\rho_v > 2/3$ and find the maximum global density where the linear regime is still valid $\rho_1^* = \gamma\rho_v = 1/3$. For densities $\rho > \rho_1^*$ jamming starts to occur and spread through the network.

For $\gamma \neq 0.5$ the network is anisotropic and the distribution of vertex densities has a finite width, so a simple analytical solution with all ρ_v equal is no longer possible. For every segment within a particular network, however, we can explicitly solve the condition $\alpha > \beta$ using matrix ϵ to find the global density ρ_1^* where jamming first occurs. Naturally, this transition density depends on the size of the network N_s and the exit probability γ (for $L \to \infty$ the length of the segment does not play a role). We have averaged the results for ρ_1^* over 200 randomly created networks for every N_s and γ. We plot the resulting transition density ρ_1^* as a function of γ in Fig. 7(a). For $\gamma = 0.5$ (isotropic network) we find $\rho_1^* = 1/3$ independent of the network size N_s, as expected. As $\gamma \neq 0.5$, ρ_1^* decreases with both network size N_s and exit probability γ.

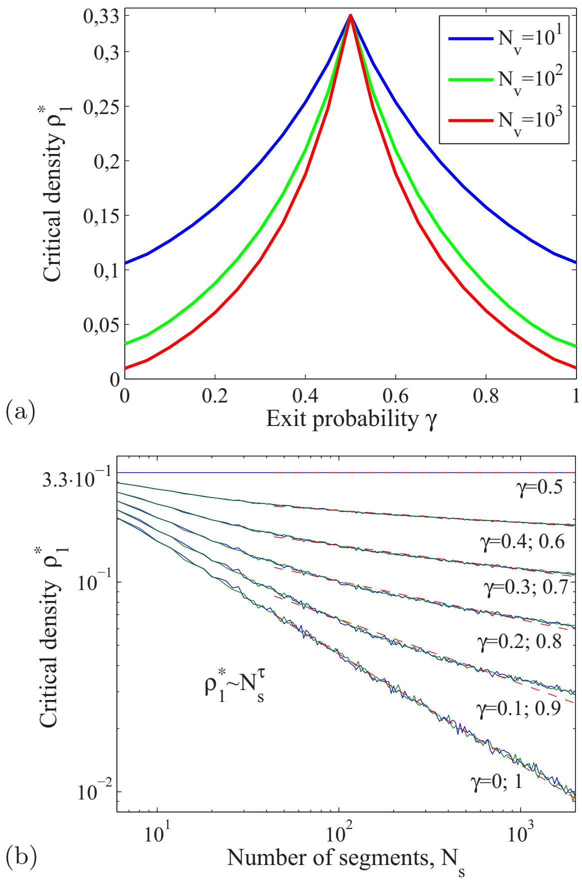

FIG. 7. (Color online) Critical density ρ_1^* demarcating the transition from the linear to the nonlinear regime. (a) Dependence of ρ_1^* on exit probability γ for several network sizes N_s. (b) Dependence of ρ_1^* on network size N_s for several exit probability γ. Blue (dark gray) curves correspond to $\gamma \leqslant 0.5$, green (light gray) curves to $\gamma > 0.5$. For each γ, the transition density can be described as a power law $\rho_1^* \approx \rho_1^0 (N_s/2)^{-|\gamma-0.5|}$ (red dashed lines).

For intermediate network sizes in the range $N_s = 3 \times 10^1 - 10^3$, we found that the power-law approximation $\rho_1^* \approx \frac{\rho_1^0}{(N_s/2)^{|\gamma-0.5|}}$ works relatively well. The prefactor $\rho_1^0 = 1/3$ for $\gamma \sim 0.5$ and is changing slightly as γ approaches 1 or 0. For $N_s = 500$ and $\gamma = 0.8$ we find $\rho_1^* \approx 0.07$, in very good agreement with Fig. 4(c). In the extreme case $\gamma = 0$ or 1, the transition density becomes simply $\rho_1^* \sim \frac{1/3}{\sqrt{N_v}}$.

For large network sizes $N_s \gtrsim 10^3$, ρ_1^* decays slower with respect to a power-law behavior. Additionally for different networks with the same N_s and γ the fluctuations of ρ_1^* can be relatively large so any analytical prediction of ρ_1^* will give only its approximate value. If one wants to know the precise value of ρ_1^*, one has to explicitly calculate it for every particular network topology using the transition matrix ϵ.

Interestingly, by analyzing the general behavior of $\rho_1^*(N_s,\gamma)$ we conclude that for sufficiently large networks ($N_s \to \infty$) and high anisotropy ($\gamma \neq 0.5$) the transition density $\rho_1^* \to 0$, meaning that local jamming and nonlinear processes start to occur at infinitely small densities.

APPENDIX C: HISTORY-DEPENDENT EXIT PROBABILITIES

In the manuscript, we have concentrated on the case that the exit probabilities at crossings are independent of the history of motor motion; i.e., that they are a fixed property of the network. In this Appendix we show the results for the alternative crossing rule that the choice of the new segment depends on the previous motion. In this case, we introduce the exit probability γ^h, with which the motor continues along the same line at a crossing; see Fig. 1(b). Consequently, with probability $1-\gamma^h$, the motor will change direction to the exit segment corresponding to another line, so the choice of the exit segment at the crossing completely depends on where the motor came from.

From the network topological perspective every crossing becomes identical and there is no fixed preferability of one segment over the other. Consequently, for all γ^h this situation is very similar to the isotropic case $\gamma = 0.5$ when motors do not have "history" of its past motion. Indeed for all investigated γ^h, we observe steady-state currents very similar to the previous case $\gamma = 0.5$ as shown in Fig. 8(a). In particular, all current distributions are symmetric with respect to $\rho = 0.5$. In fact, for $\gamma = 0.5$ and $\gamma^h = 0.5$ we get identical transport behavior in the network with current plateau for densities in the range $1/3 < \rho < 2/3$. Increasing γ^h above 0.5 makes the equilibration time to reach the steady state longer due to stronger local fluctuations between the segments. We find that these stronger fluctuations also lead to slight decrease of the maximum current; see Fig. 8(b). This current reduction is, however, much weaker (almost negligible, only ∼3%) than the one described in the main manuscript for the case of history-independent exit probabilities.

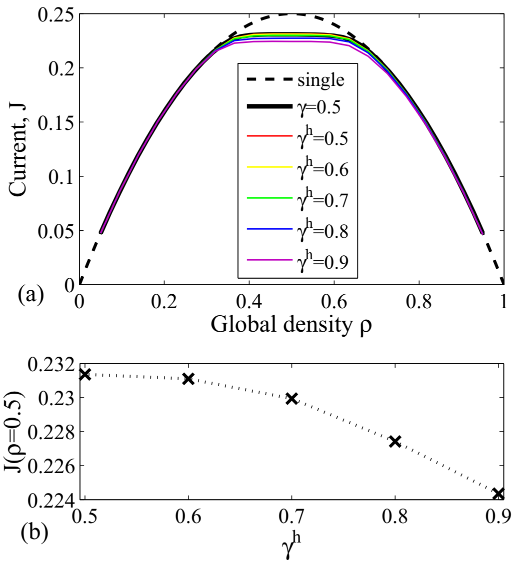

FIG. 8. (Color online) (a) Transport current J dependence on exit probability γ^h for different densities ρ. Black dashed curve corresponds to the single segment behavior, while black solid curve corresponds to $\gamma = 0.5$ when the choice of the new segment is independent on the past motor motion. Colored curves correspond to the case $\gamma^h = 0.5$, 0.6, 0.7, 0.8, and 0.9 when the choice the new segment depends on the incoming segment (see legend). (b) Decrease of the optimal current value at $\rho = 0.5$ with increasing γ^h.

[1] S. Ramaswamy, Annu. Rev. Condens. Matter Phys. **1**, 323 (2010).

[2] M. C. Marchetti, J. F. Joanny, S. Ramaswamy, T. B. Liverpool, J. Prost, M. Rao, and R. A. Simha, Rev. Mod. Phys. **85**, 1143 (2013).

[3] D. A. Head, A. J. Levine, and F. C. MacKintosh, Phys. Rev. Lett. **91**, 108102 (2003).

[4] Edited by M. R. K. Mofrad and R. D. Kamm, *Cytoskeletal Mechanics* (Cambridge University Press, Cambridge, 2006).

[5] C. P. Brangwynne, G. H. Koenderink, F. C. MacKintosh, and D. A. Weitz, Trends Cell Biol. **19**, 423 (2009).

[6] J. L. Ross, M. Y. Ali, and D. M. Warshaw, Curr. Opin. Cell Biol. **20**, 41 (2008).

[7] F. Huber, A. Boire, M. Preciado Lopez, and G. H. Koenderink, Curr. Opin. Cell Biol. **32**, 39 (2015).

[8] M. Preciado-Lopez *et al.*, Methods Enzymol. **540**, 301 (2014).

[9] C. T. MacDonald, J. H. Gibbs, and A. C. Pipkin, Biopolymers **6**, 1 (1968).

[10] C. T. MacDonald and J. H. Gibbs, Biopolymers **7**, 707 (1969).

[11] A. Parmeggiani, T. Franosch, and E. Frey, Phys. Rev. Lett. **90**, 086601 (2003).

[12] I. Neri, N. Kern, and A. Parmeggiani, Phys. Rev. Lett. **107**, 068702 (2011).

[13] I. Neri, N. Kern, and A. Parmeggiani, Phys. Rev. Lett. **110**, 098102 (2013).

[14] E. Frey, A. Parmeggiani, and T. Franosch, Genome Inf. **15**, 46 (2004).

[15] J. L. Ross, H. Shuman, E. L. F. Holzbaur, and Yale E. Goldman, Biophys. J. **94**, 3115 (2008).

[16] S. Verbrugge, S. M. van den Wildenberg, and E. J. Peterman, Biophys. J. **97**, 2287 (2009).

[17] L. Conway, D. Wood, E. Tuzel, and J. L. Rossb, Proc. Natl. Acad. Sci. USA **109**, 20814 (2012).

[18] R. P. Erickson, S. P. Gross, and C. C. Yu, PLoS ONE **8**, e54298 (2013).

[19] H. W. Schroeder, A. G. Hendricks, K. Ikeda, H. Shuman, V. Rodionov, M. Ikebe, Y. E. Goldman, and E. L. Holzbaur, Biophys. J. **103**, 48 (2012).

[20] A. Raguin, A. Parmeggiani, and N. Kern, Phys. Rev. E **88**, 042104 (2013).

[21] B. Embley, A. Parmeggiani, and N. Kern, Phys. Rev. E **80**, 041128 (2009).

[22] For sufficiently long segments ($L \geqslant 200$) the density and current of a segment are fully determined by the inflow and outflow at the boundaries and does not depend on L.

[23] The choice of the new segment may also depend on the current segment but this is second-order effect comparing to the local topology that we neglect in the current manuscript. Moreover, taking into account switching rules which depends on the incoming segment will make the current and density

distribution more homogenous but will not add new features; see Appendix C.

[24] I. A. Telley, P. Bieling, and T. Surrey, Biophys. J. **96**, 3341 (2009).

[25] To neglect the effect of binding and unbinding one can think not in terms of single motors traveling along the network but rather in terms of the cargos being transported along the microtubules by several motors at once. In this case the chace for the cargo to unbind is relatively small even if one of transporting motor unbinds.

[26] B. Derrida, E. Domany, and D. Mukamel, J. Stat. Phys. **69**, 667 (1992).

[27] M. Gerwinski and J. Krug, Phys. Rev. E **60**, 188 (1999).

[28] D. M. Miedema, A. S. de Wijn, and P. Schall, Phys. Rev. E **89**, 062812 (2014).

[29] J. D. Noh and H. Rieger, Phys. Rev. Lett. **92**, 118701 (2004).

[30] B. Tadić, Eur. Phys. J. B **23**, 221 (2001).

[31] M. Andjelkovic, N. Gupte, and B. Tadić, Phys. Rev. E **91**, 052817 (2015).